Quantum Science and Technology

Yoshiro Hirayama
Koji Ishibashi
Kae Nemoto *Editors*

Hybrid Quantum Systems

Springer

Quantum Science and Technology

The book series Quantum Science and Technology is dedicated to one of today's most active and rapidly expanding fields of research and development. In particular, the series will be a showcase for the growing number of experimental implementations and practical applications of quantum systems. These will include, but are not restricted to: quantum information processing, quantum computing, and quantum simulation; quantum communication and quantum cryptography; entanglement and other quantum resources; quantum interfaces and hybrid quantum systems; quantum memories and quantum repeaters; measurement-based quantum control and quantum feedback; quantum nanomechanics, quantum optomechanics and quantum transducers; quantum sensing and quantum metrology; as well as quantum effects in biology. Last but not least, the series will include books on the theoretical and mathematical questions relevant to designing and understanding these systems and devices, as well as foundational issues concerning the quantum phenomena themselves. Written and edited by leading experts, the treatments will be designed for graduate students and other researchers already working in, or intending to enter the field of quantum science and technology.

More information about this series at https://link.springer.com/bookseries/10039

Yoshiro Hirayama · Koji Ishibashi · Kae Nemoto
Editors

Hybrid Quantum Systems

Springer

Editors
Yoshiro Hirayama
Center for Science and Innovation
in Spintronics
Tohoku University
Sendai, Miyagi, Japan

Koji Ishibashi
Advanced Device Laboratory
RIKEN
Wako, Saitama, Japan

Kae Nemoto
Principles of Informatics Research Division
National Institute of Informatics
Tokyo, Japan

Ministry of Education, Culture, Sports, Science and Technology

ISSN 2364-9054 ISSN 2364-9062 (electronic)
Quantum Science and Technology
ISBN 978-981-16-6678-0 ISBN 978-981-16-6679-7 (eBook)
https://doi.org/10.1007/978-981-16-6679-7

This Springer imprint is published by the registered company Springer Nature Singapore Pte Ltd.
The registered company address is: 152 Beach Road, #21-01/04 Gateway East, Singapore 189721, Singapore

Preface

Together with about 50 scientists around Japan, we pursued the basic science of hybrid quantum systems under the framework of the project "Science of Hybrid Quantum Systems" (HQS). This project was started in July 2015 as part of a Grant-in-Aid for Scientific Research on Innovative Areas, organized by MEXT (the Ministry of Education, Culture, Sports, Science and Technology) in Japan. The main streams of quantum science and quantum technology at that time were focused around quantum information processing, such as quantum cryptography, the realizations of qubits on a number of different physical systems such as superconductivity, electron spin, and atom and ion traps, and the integration of these qubits toward quantum computers. The project began with the finding that there was an approach distinctly different from a path of integration of the same type of qubits, and this approach would have potentials to lead us to a new landscape of quantum science. Even with a small number of qubits, we can achieve unprecedented sensor sensitivity. By developing quantum transducers with different physical quantities, we can exchange quantum information on different scales such as energy and distance. We investigated the quantum coupling between different physical quantities, such as charges, Cooper pairs, electron spins, nuclear spins, photons, and phonons, aiming to impact a wide range of fields from science and engineering to medicine.

Significant effects and interesting results have been obtained over the 5 years of the project, and many collaborations began and have flourished, even continuing beyond the end of the project. We are planning to publish two books ("Hybrid Quantum Systems" and "Quantum Hybrid Electronics and Materials") from Springer Nature to summarize our progress and to broadly discuss the importance of this hybridization work.

This book, “Hybrid Quantum Systems”, summarizes results related to quantum transducers, quantum sensing using coherent spin operation, and theoretical studies on hybrid quantum systems. There are many stimulating chapters discussing the various hybrid systems in which charges, spins, nuclear spins, photons, and phonons are coherently coupled.

We hope this book will help you understand the interest, importance, and diversity of “Hybrid Quantum Systems”.

Finally, we are grateful to the members of the Editorial Office of Springer-Nature Publishing for their excellent help. We would also like to thank all the individual authors for their significant efforts.

Sendai, Japan — Prof. Yoshiro Hirayama
Wako, Japan — Prof. Koji Ishibashi
Tokyo, Japan — Prof. Kae Nemoto

Contents

Control of Spin Coherence and Quantum Sensing in Diamond

Norikazu Mizuochi

Abstract Quantum superposition, namely coherence, is fundamentally important in quantum science. It is not easy to maintain it for a long time because it is very sensitive to environmental noises. Quantum sensing utilizes this character to realize high sensitivity. Therefore, control of coherence is a central issue in quantum technology. In this chapter, we mainly present recent our researches about the extension of coherence times of NV centers in diamond (1.1), electrical control and detection of spin coherence in diamond (1.2), and quantum hybrid sensors in diamond (1.3). In section (1.1), researches of the extension of coherence times of the NV centers by utilizing n-type diamond and a quantum hybrid system of dressed states are presented. Recently, we realized the longest inhomogeneous spin-dephasing time ($T_2{}^* \approx 1.5$ ms) and Hahn-echo spin-coherence time ($T_2 \approx 2.4$ ms) of single electron spins in NV centres, ever observed in room-temperature solid-state systems. In section (1.2), an electrical control for extension of coherence times and electrically detected magnetic resonance are presented. The latter is the first demonstration of room-temperature electrical detection of nuclear spin coherence in diamond and any other materials. In section (1.3), quantum hybrid sensors in diamonds are presented. Furthermore, the investigation of the magnetic resonance spectrum of a high-density ensemble of the NV centers, which is required for ultra-high sensitivity, is presented by introducing an appropriate model. By adopting this model, we estimated the optimal temperature sensitivity with the appropriate concentration of the NV centers.

Keywords Diamond · NV center · Quantum sensor · Dressed state

1 Extension of Coherence Times of NV Centers in Diamond

Solid-state spins are a leading contender in quantum technology [1]. Enhancing the inhomogeneous spin-dephasing time ($T_2{}^*$) and the Hahn-echo spin-coherence time (T_2) is a central issue. The electron spin plays a significant role for quantum

N. Mizuochi (✉)
Institute for Chemical Research, Kyoto University, Kyoto, Japan
e-mail: mizuochi@scl.kyoto-u.ac.jp

Y. Hirayama et al. (eds.), *Hybrid Quantum Systems*, Quantum Science and Technology,
https://doi.org/10.1007/978-981-16-6679-7_1

sensing and for coherent connectivity with other qubits such as photons [2–4], nuclear spins [5–7], and superconducting qubits [8, 9]. Therefore, the coherence times define the physical behavior of the quantum device, and their improvement allows new perspectives for quantum applications. For example, their increase directly improves direct current (DC) and alternating current (AC) sensitivities of nitrogen-vacancy (NV) sensors [10, 11] quantum-gate fidelity [12, 13], and quantum-memory times [10, 12, 14, 15].

The extension of the spin coherence time has been demonstrated by suppressing noises with various techniques such as tailored dynamical decoupling [16–18], measurements at low temperature [19], measurements at high magnetic field [20], and decoupling by fast charge-state changes with high power laser irradiation [21] in addition to removal of noise sources by growth techniques [10, 14, 22, 23].

From the viewpoint of material science, enhancements of T_2^* and T_2 have been realized by the development of growth techniques to suppress paramagnetic defects [24], isotope engineering to reduce nuclear spins [10, 12, 22], and annealing techniques to remove defects [25]. Regarding diamond crystals, there has been remarkable progress in the quality of single crystal diamond grown by chemical vapour deposition (CVD). By suppressing impurities and defects, the T_2 of NV centres has been enhanced. For example, $T_2 = 0.7$ ms is reported, which is the longest T_2 at room temperature amongst diamonds which contain a natural abundance (1.1%) of ^{13}C [22, 26]. Furthermore, by depleting the ^{13}C isotope, the electron spin showed significantly long room-temperature spin-dephasing times ($T_2^* = 100$ μs [27], 470 μs [21]) and spin-coherence times ($T_2 = 1.8$ ms in single-crystal [10] and 2.0 ms in poly-crystal diamond [28]).

In principle, T_2 can be extended closer to T_1 (~6 ms [5]), however, this has not been reached yet. The reason considered is the effect of residual paramagnetic defects and/or impurities in the bulk. During the CVD growth [29] and ion-implantation [30], it is known that many vacancies are generated. Once they combine, complexes or defect clusters are formed. It is very hard to remove them by annealing techniques because they are very stable. Therefore, the longest T_2^* and T_2 of single NV centres have been realized by native NV centres created during CVD growth, while those of NV centres created by ion-implantation and a high annealing temperature have not exceeded the longest ones.

1.1 Long Coherence Times and High Magnetic Sensitivity with NV Centres in Phosphorus-Doped n-type Diamond

Extending coherence times is rather challenging. Although enrichment of the spin-zero ^{12}C and ^{28}Si isotopes greatly reduces spin-bath decoherence in diamond and silicon, the solid-state environment provides undesired interactions between the electron spin and the remaining spins of its surrounding. Here we demonstrate,

contrary to widespread belief, that an impurity-doped (phosphorus) n-type single-crystal diamond realizes remarkably long spin-coherence times [14]. Single electron spins show the longest inhomogeneous spin-dephasing time ($T_2^* \approx 1.5$ ms) and Hahn-echo spin-coherence time ($T_2 \approx 2.4$ ms) ever observed in room-temperature solid-state systems, leading to the best sensitivities. The extension of coherence times in diamond semiconductors may allow for new applications in quantum technology.

Recently, charging of vacancies suppressed the formation of vacancy complexes by confining implantation defects into a space-charge layer of free carriers created by a thin sacrificial boron-doped p-type diamond layer [30]. After removing this layer, the T_2 of the NV centres at the shallow surface region was improved only. In their research, the intrinsic diamond was used, but n-type conductivity is crucially important because of the stabilization of the negatively charged state of the NV centres (NV^-) [31, 32], and because of the electrical controls used in diamond quantum devices.

1.1.1 Sample and Doping Concentration Comparison

The n-type diamond samples A ~ H were grown onto Ib-type (111)-oriented diamond substrates by microwave plasma-assisted CVD with enriched C (99.998%) and with phosphorus concentrations ranging from 3×10^{15} to 1×10^{17} atoms/cm^3. For all samples, the growth conditions are the same except for the PH_3/CH_4 gas ratio to change the phosphorus concentration. We address individual NV centres with a home-built confocal microscope. All experiments were conducted at room temperature.

In order to compare the doping concentrations, two parameters were measured for a number of NV centres in every sample: the population of the NV^- state, and T_2. The NV^- population is determined by single-shot charge-state measurements, and T_2 with a Hahn-echo measurement. The results of samples A ~ H are plotted in Fig. 1.1. In the highly doped diamond samples C ~ H, a charged state of NV^- near 100% is realized, while, regardless of the paramagnetic dopant (electron spin 1/2), T_2 can surpass 2 ms. The different local surroundings of each NV centre are considered to be the reason for the scatter of T_2 for each NV^- population. NV centres with a higher NV^- population show a longer maximum T_2. Moreover, sample C with [P] $= 6 \times 10^{16}$ atoms/cm^3 seems to produce NV centres with longer T_2 than diamond with both smaller and larger phosphorus concentrations, with an average over the first 21 measured NV centres of $\langle T_2 \rangle = 1.8$ ms and almost 40% has $T_2 > 2.0$ ms. This might indicate a competition between a positive effect of phosphorus doping and the negative effect of magnetic noise stemming from phosphorus, and therefore an optimum concentration could exist.

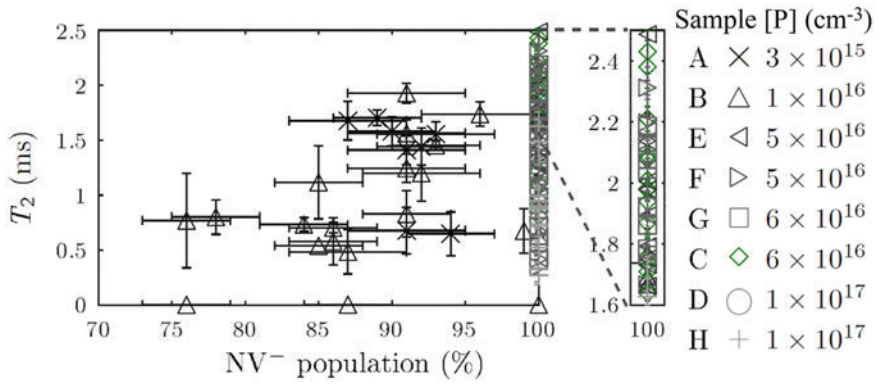

Fig. 1.1 T_2 vs NV population for eight samples A ~ H with different doping levels: 3×10^{15} (crosses), 1×10^{16} (up-pointing triangles), 5×10^{16} (left and right-pointing triangles), 6×10^{16} (squares and diamonds), and 1×10^{17} atoms/cm^3 (circles and pluses). The error bars indicate standard errors. The top-right of the graph is enlarged

1.1.2 Coherence Times

Owing to the pure NV^- state and long T_2, sample C with $[P] = 6 \times 10^{16}$ atoms/cm^3 was investigated more in-depth. At first, T_2^* was studied, measured via the exponential decay of a free induction decay (FID) measurement. Since it is hard to measure T_2^* due to the strong effect of the environment, the measurement time is decreased by using both short and long delays in one measurement sequence, resulting in $T_2^* = 1.54$ ms. Compared with the previously reported long T_2^* of phosphor in an isotopically engineered ^{28}Si crystal (270 μs) and of NV centres in diamond (470 μs), this is the longest T_2^* for an electron spin ever observed in solid-state systems. The DC magnetic field sensitivity of the single NV centre can be derived to be ~6 nT/(Hz)$^{1/2}$.

To find NV centres with a long T_2, Hahn-echo measurements were conducted for the ones with a long T_2^*. Measurements for the $M_S = 0$ state and the $M_S = 1$ state were subtracted and normalised to reject common-mode noise, and the result was fitted to the exponential exp $(-(Delay/T_2^*))$. Figure 1.2c shows the longest T_2 consistently measured (2.43 ms), which is the longest T_2 for an electron spin ever observed in solid-state systems at room temperature. In these references, as opposed to our results, the measurements are performed without common-mode noise rejection, the results are rather noisy, and n was fixed at 2 for the fits. Hence, the uncertainty in T_2 decreases (since T_2 and n appear in the same exponent only), and the fitted T_2 increases (since for long T_2, generally $n < 2$; for our measurement, forcing $n = 2$ gives $T_2 = 2.93$ ms). Moreover, as visible in Fig. 1.2b, even the average $<T_2> = 1.8$ ms of our measured NV centres rivals with the longest T_2 measured in single-crystal diamond ($T_2 = 1.8$ ms), and almost 40% are longer than the longest T_2 measured in poly-crystal diamond ($T_2 = 2.0$ ms), while both references only show their best measurement.

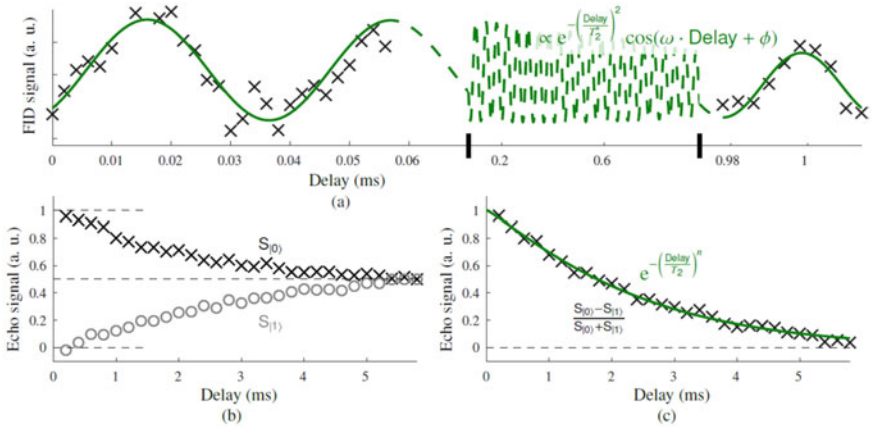

Fig. 1.2 T_2^* and T_2 in sample C. **a** Result of FID measurement (data with crosses, sinusoidal exponential-decay fit with line, $T_2^* = 1.54$ ms). Please note the breaks on the horizontal axis; all data are fitted with a single function. **b** Results for the $S_{|0\rangle}$ measurement (crosses) and for the $S_{|1\rangle}$ measurement (circles). The top and bottom dashed lines correspond to a maximum population of the |0> and |1> states respectively. The middle dashed line is when both states are populated equally. **c** Echo signal derived from subtracting (b)'s $S_{|0\rangle}$ (data with crosses, exponential-decay fit with line, $T_2 = 2.43$ ms). The dashed line at 0 indicates when the states are populated equally

1.1.3 Sensitivity

Since the AC magnetic field sensitivity is proportional to $1/(T_2)^{1/2}$, the NV centre with the longest T_2 was examined. The concept for the measurement is based on the oscillation of the population of the spin state with the magnetic field amplitude (B_{AC}). Therefore, to measure B_{AC}, a working point of maximum gradient is chosen (the dashed lines in Fig. 1.3a), and then the Hahn-echo intensity is measured. Via the gradient, this intensity relates directly to B_{AC}.

The sensitivity is $\eta = \delta B_{\min}(T_{\text{meas}})^{1/2}$ with $\delta B_{\min}$ the minimum detectable magnetic field amplitude, and T_{meas} the measurement time. $\delta B_{\min}$ relates directly to the uncertainty of the measurement, and is given by $\delta B_{\min} = \sigma_1/\text{grad}$ with σ_1 the uncertainty of a single Hahn-echo measurement and grad the gradient in the working point. Since σ_1 depends on the noise in the system, which generally scales over measurement time with $1/(T_{\text{meas}})^{1/2}$, the sensitivity is independent of the measurement time, hence its usefulness for comparing systems. Also, please be aware that the sensitivity of a measurement should be determined in the same way the measurement itself is conducted, thus a technique such as used here is the only correct way to obtain a sensitivity.

To obtain the optimum sensitivity, first, the T_2 data are used to estimate the optimum magnetic field frequency for the measurement, which is $f_{AC} = 833$ Hz. Next, the gradient in the working point was determined. Since this is a constant given the measurement parameters and environment, a relatively long time averaging measurement can be used. An average result is shown in Fig. 1.3a, which gives grad

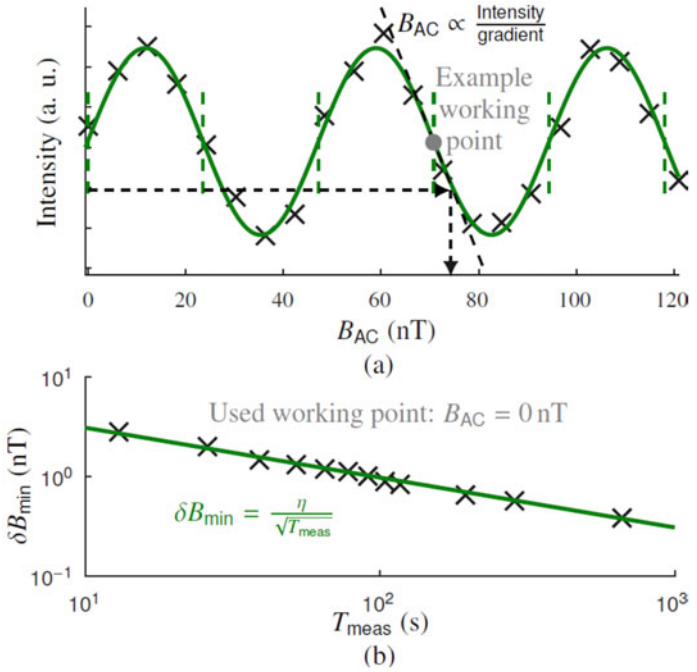

Fig. 1.3 AC magnetic field measurement. **a** Single measurement to find the working points which have the maximum gradient (100 000 iterations, data with crosses, sinusoidal fi with line). The working point indicated with a circle is an example, the dashed arrows show how a measured intensity translates to a magnetic field amplitude. **b** Logarithmic plot of δB_{min} versus T_{meas}

$= 1.56 \times 10^7$ intensity T^{-1}. Next, the uncertainty of a measurement in the working point is extracted by measuring this point 100 times for a number of measurement times T_{meas} ranging from 13 s to 11 min. In Fig. 1.3b, the resulting δB_{min} is fitted to $\eta/(T_{meas})^{1/2}$, from which follows the sensitivity $\eta = 9.1$ nT/(Hz)$^{1/2}$.

1.1.4 Discussion

The AC magnetic field sensitivity is improved by almost a factor of two compared to previous results. The reasons for this improvement are the longer T_2, the larger Rabi contrast and the slightly higher photon count due to n-type diamond.

That the doping of phosphorus extends the spin-coherence times and gives better magnetic field sensitivities is against intuition, because phosphorus is paramagnetic at room temperature in diamond due to a large activation energy of 0.57 eV, and thus causes magnetic noise. The time extensions in n-type diamond are considered to be due to charging of the vacancies, which suppresses the formation of paramagnetic vacancy complexes during growth. Potentially, this mechanism is similar to

the recently reported interpretation of suppression of vacancy creation during ion-implantation through a sacrificial boron-doped p-type layer. During the CVD growth, it is known that many vacancies are generated, which causes generation of thermally stable impurity-vacancy and multi-vacancy complexes. However, their generation can be suppressed by Coulomb repulsion of charged vacancies in n-type diamond, where an accepter level of the vacancy is located at 2.6 eV below the conduction band, which is lower than the donor level of phosphorus (0.57 eV). For a two-level system, T_2 is known to be ultimately limited by the longitudinal spin-relaxation time T_1. We applied Carr-Purcell- Meiboom-Gill (CPMG) dynamic-decoupling sequences with common-mode noise rejection, and $T_{2dd} = 3.3$ ms was derived. Although T_{2dd} is longer than T_2, it is still shorter than T_1 (6~7.5 ms). To obtain information about the sources of decoherence, we carried out noise spectroscopy and T_1 measurements.[Dav].

The noise spectrum of deep NV centres can be analyzed by a single Lorentzian. For our data (see Fig. 1.4), since the cut-off frequency eludes us, we fixed it as the highest probed frequency (thus $\tau_c < 0.25\ \mu s$), and fitted to find the minimum for Δ ($\Delta > 0.1$ MHz). The minimum density of the paramagnetic impurities/defects n_{para} was derived from Δ under the assumption that the noise source originates from dipolar interaction between these and the NV centre only ($n_{para} \sim \Delta/\alpha$ with $\alpha = 3.3 \times 10^{-13}$ cm^3/s), giving 3×10^{17} cm^{-3}, which is much larger than doped P.

For a Lorentzian bath, in the limit of very short correlation times ($\tau_c \ll T_2$), the dynamical-decoupling sequence is inefficient and there is no improvement with the number of pulses. In addition, there is a limitation to the π-pulse duration, and their spacing restricts the maximum CPMG filter frequency. We consider that these explain why the decoupling technique is not very effective for the extension of T_2.

As for the contribution of nuclear spins, from the applied external magnetic field (1.8 mT), the Larmor frequencies of the nuclear spins of ^{14}N, ^{15}N, ^{13}C, ^{31}P, and ^{1}H were calculated and they are indicated in Fig. 1.4. They were not detected in the noise spectrum, which indicates as well that the contribution of the nuclear spins to the decoherence is small.

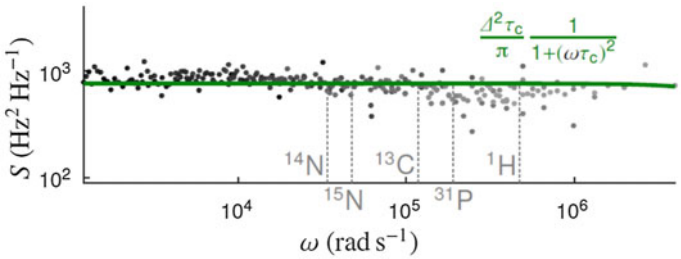

Fig. 1.4 Noise spectrum extracted from dynamic-decoupling measurements (with 2^n pulses with $n = 1 \sim 9$, data with dots, Lorentzian fit with line, correlation time τ_c fixed to represent the highest probed frequency). The Larmor frequencies of several nuclear spins are indicated (dashed lines); $B = 1.8$ mT

1.2 *Extension of the Coherence Time by Generating MW Dressed States in a Single NV Centre in Diamond*

Here, we focus on the microwave (MW) dressed state based on Autler-Townes splitting (ATS). Using ATS, a large number of the dressed states can be generated. It has also been reported that T_2 of the MW dressed states is longer than that of undressed states. In this research [33], we experimentally demonstrate the generation of the MW dressed states in the single NV centre in diamond by ATS at ambient conditions in order to analyse fundamental phenomena. We show the extension of T_2 under the generation of the dressed states.

Mechanism of Autler-Townes Splitting

Figure 1.5a shows the energy level of the NV electron spin coupled with the ^{14}N nuclear spin of the NV centre, where $|m_s, m_I\rangle$ is defined as the electron and the ^{14}N nuclear spin of the NV centre, respectively. After laser illumination, the NV centre is equally polarised in $|0,0\rangle$, $|0,1\rangle$, and $|0,-1\rangle$ depicted by the open circles under the application of a static magnetic field (B_0). Figure 1.5a also depicts the irradiation of an unperturbed drive field whose frequency is close to a resonant frequency of a transition between $|0,1\rangle$ and $|-1,1\rangle$. When the drive field is considered as a classical mw mode, the NV centre can be coupled to the mode of the drive field. Then, each $|0,1\rangle$ and $|-1,1\rangle$ is split into two levels described in Fig. 1.5b. As an example, Fig. 1.5b depicts the generation of four dressed states of $|0,1\rangle|1\rangle$, $|-1,1\rangle|0\rangle$, $|0,1\rangle|2\rangle$, and $|-1,1\rangle|1\rangle$ in the presence of coupling between the NV centre ($|0,1\rangle$ and $|-1,1\rangle$) and the mode of the drive field ($|0\rangle$, $|1\rangle$, and $|2\rangle$). This phenomenon is called (weak) ATS. Figure 1.5b also shows the energy levels of the dressed states which are characterised by the Rabi frequency of an NV electron spin (Ω) and frequency of the drive field (ω).

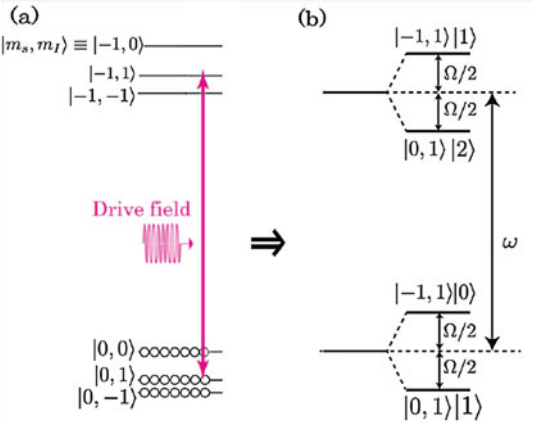

Fig. 1.5 **a** Energy diagram of the NV centre under irradiation of a weak drive field. **b** Dressed energy level coupling with a mode of the drive field

Results and Discussion

The sample is a type IIa (111) diamond. In our experiment, we chose an NV centre that is weakly coupled to other nuclear spins (e.g., ^{13}C nuclear spin). We measured the optically detected magnetic resonance (ODMR) spectrum with a 1-μs pulsed laser by sweeping the frequency of a 5.5-μs pulsed probe MW (Pmw) pulse (π pulse) depicted top of Fig. 1.6. In Fig. 1.6a, the ODMR spectrum has three dips with 2.1 MHz splitting, which corresponds to the hyperfine splitting of the ^{14}N nuclear spin of the NV centre.

Experimental Generation of Dressed States by ATS

First, we measured the change in the dressed-state resonant frequencies by changing the power of continuous drive MW (D_{mw}) with pulse sequence depicted in the top of Fig. 1.6. These experiments use the three D_{mw} frequencies of 2834.75 MHz ($D_{mw}1$), 2837.05 MHz ($D_{mw}2$), and 2839.18 MHz ($D_{mw}3$) to generate dressed states. The results are shown in Fig. 1.6b. The signals for each D_{mw} frequency split into three above ~10 μT.

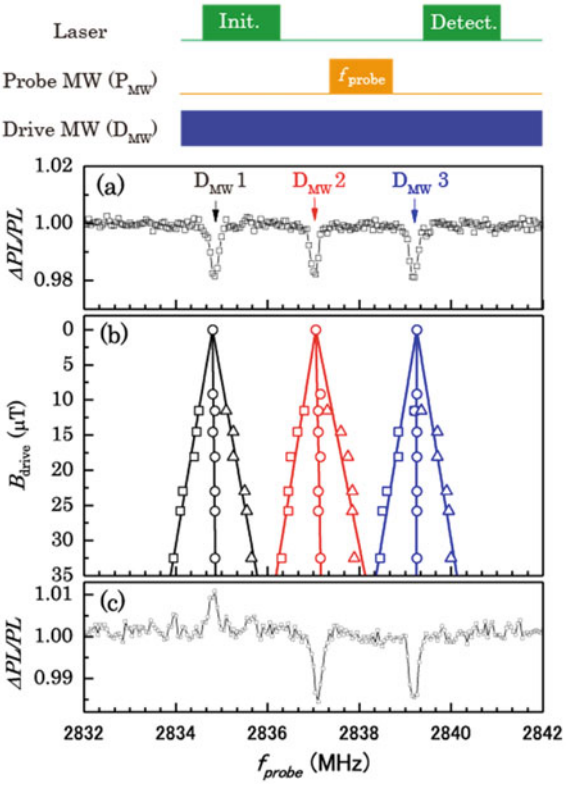

Fig. 1.6 **a** ODMR spectrum without any drive fields. **b** Resonant frequencies as a function of the strength of the drive field (B_{drive}). Black, red, and blue plots show the changes in resonant frequencies under the irradiation of D_{mw} frequencies of 2834.75 MHz (D_{mw} 1), 2837.05 MHz (D_{mw} 2), and 2839.18 MHz (D_{mw} 3), respectively. Solid lines are fitted for each resonant frequency. **c** ODMR spectrum under a D_{mw} at a frequency of 2834.75 MHz and a D_{mw} power of 33 μT. We can observe the Mollow triplet, which we call ATS

Here we focus on the 2834.75 MHz of $D_{mw}1$. It should be noted that all three D_{mw} frequencies have the same dependences on the power of the continuous D_{mw}. The ODMR spectrum under continuous irradiation at $D_{mw}1$ with the power of 33 μT is shown in Fig. 1.6c. Figure 1.6c shows the ODMR spectrum at ~2834.75 MHz splits into three peaks under the irradiation of the D_{mw}. Figure 1.6b shows that the resonant frequencies of the dressed states as a function of B_{drive}. The solid lines show the linear fitting for each observed data. The absolute values of these slopes in Fig. 1.6b agree well with the gyromagnetic ratio of the NV electron spin (γ_{NV}), so that means the resonant frequencies of side peaks are linearly proportional to the Rabi frequencies of the NV electron spin. These our results are consistent with the theoretical prediction in ATS, demonstrating the generation of more than four dressed states by the ATS [33].

Coherence Time of Dressed States

First, in order to investigate the magnetic moments of the dressed and undressed states, we measured Rabi oscillations of the dressed states and the NV electron spin as described in Ref. [33]. The result indicates the Rabi frequency of the dressed spin states is the same with that of undressed spin states [33]. Consequently, the magnetic moment of the NV electron spin and the dressed states are the same with each other.

Next, we measured coherence time of the dressed states ($T_{2\rho}$) and T_2 of a single NV centrein a ^{12}C enriched diamond. The top of Fig. 1.7 shows the pulse sequence for the $T_{2\rho}$ and T_2 measurements. It is noted that while $T_{2\rho}$ was measured with the continuous D_{mw} irradiation, T_2 was measured without continuous D_{mw} irradiation. Since the pulsed laser and continuous D_{mw} were simultaneously irradiated to the NV centre during the $T_{2\rho}$ measurements, we kept the pulse sequence time (T_{seq}) constant adjusting interval between the final $\pi/2$ P_{mw} pulse and the readout laser pulse depicted in Fig. 1.7. Then, the dressed spin states can be initialised by simultaneous irradiation of the pulse laser and the continuous D_{mw} in the $T_{2\rho}$ measurements. Additionally,

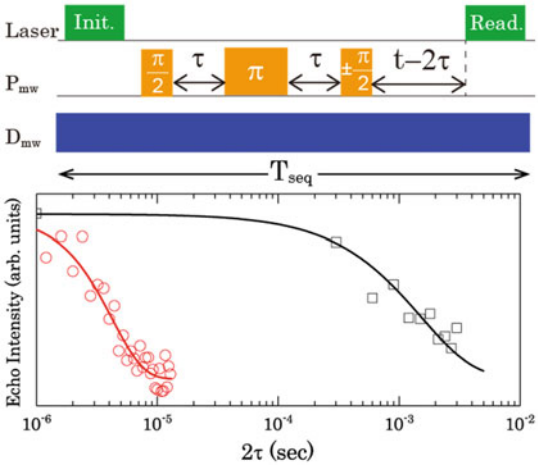

Fig. 1.7 (Top) Pulse sequence to observe $T_{2\rho}$ and T_2 with applying a phase cycle to the final $\pi/2$ pulse. (Bottom) Black and red plots show the results of $T_{2\rho}$ and T_2 measurements, respectively. They are fitted by exponential decay curves described by black and red solid lines

a phase cycling technique was applied to $T_{2\rho}$ measurements in order to remove common-mode noise from laser fluctuations. In the case of a P_{mw} and D_{mw} strength of ~0.43 MHz and ~1.2 MHz, respectively, the result of $T_{2\rho}$ (black plots) and T_2 (red plots) measurements fitted with exponential decay curves are shown in Fig. 1.7. The results show that we observed a coherence time of $T_{2\rho} \sim 1.5$ ms of the dressed states, which is more than two orders of magnitude longer than $T_2 \sim 4.2$ μs of the undressed states. While such an extension can also be demonstrated by a dynamical decoupling technique, e.g., a CPMG sequence in the NV centres, an extension of two orders of magnitude by the ATS is much larger than the extension of about one order of T_2 in the dynamical decoupling techniques. The extended T_2 by the ATS is also close to the longest T_2 of a single NV centre in a ^{12}C enriched diamond.

Related Research About Dressed State: Experimental Demonstration of Two-Photon Magnetic Resonances in a Single-Spin-System of a Solid

In the research described at previous section, the dressed states among the electron spin with microwave were generated. In addition, we investigated dressed states including nuclear spins by introducing a radio frequency (rf). In this experimental demonstration, we used the electron spin and the ^{14}N nuclear spin of the NV center to generate the dressed states [34].

While the manipulation of quantum systems is significantly developed so far, achieving a single-source multi-use system for quantum-information processing and networks is still challenging. A virtual state, a so-called "dressed state," is a potential host for quantum hybridizations of quantum physical systems with various operational ranges. We present an experimental demonstration of a dressed state generated by two-photon magnetic resonances using a single spin in a single NV center in diamond. The two-photon magnetic resonances occur under the application of microwave and radio-frequency fields, with different operational ranges. The experimental results reveal the behavior of two-photon magnetic transitions in a single defect spin in a solid, thus presenting new potential quantum and semi-classical hybrid systems with different operational ranges using superconductivity and spintronics devices.

We discussed the strategy for generating a hybrid system with a generated dressed state. Trifunovic et al. [35] have proposed a hybrid strategy between magnetic materials and electron spin in NV centers in diamond using dipole coupling for a fusion of classical and quantum information processing. In this case, our demonstration of two-photon magnetic resonance (TPMR) indicates that we can hybridize these spins with wide-range operational fields through an NV center because we can optimize the parameters for coupling between both spins in both the mw and rf operational fields. We clearly observed the generated dressed states using TPMRs via the single-defect spin in diamond. We showed that the generated dressed states can be converted reversibly by driving both fields. These results indicate the potential for hosting hybridizations of physical systems with different operational ranges. Thus, our results pave the way for a new fusion of physical systems with single qubits and wide operational ranges.

2 Electrical Control and Detection of Spin Coherence in Diamond

2.1 Electrical Control for Extension of Spin Coherence Times of NV Centers in Diamond

The extension of the spin coherence times has been demonstrated by suppressing noises with various techniques such as, dynamical decoupling, measurements at low temperature, measurements at high magnetic field, and decoupling by fast charge-state changes with high power laser irradiation in addition to removal of noise sources by growth techniques. On the other hand, realization of the suppression by an electric field is important because the electric field can be locally operated in individual on-chip nanoscale devices such as scalable quantum device in a dense array and quantum nanoscale sensing device. Furthermore, it does not need huge energy consumption facilities for operation and rare materials synthesized by isotopes without a nuclear spin.

The electrical control is challenging because the electric fields do not couple directly to the spin unlike the magnetic field. Previously, the static electric field dependence on magnetic resonance frequencies of the NV center was reported [36]. By using the dependence, application of the NV center to the nanoscale electric field sensors was demonstrated [37, 38]. In the previous research [37], the analysis of the electronic structure of the NV center reveals how an applied magnetic field influences the electric-field-sensing properties. In this study [39], coherence times, which were estimated from a free-induction-decay ($T_2{}^{\mathrm{FID}}$) and a Hahn-echo decay ($T_2{}^{\mathrm{echo}}$), were measured under the externally applied static electric fields. We report the increase of $T_2{}^{\mathrm{FID}}$ and $T_2{}^{\mathrm{echo}}$ under the electric field and discuss the mechanism.

The basic idea is as follows. The Hamiltonian is expressed as

$$\begin{aligned} H_{gs} =& \frac{1}{\hbar^2}\left(D_{gs} + d_{gs}^{\parallel} E_z\right)\left[S_z^2 - \frac{1}{3}S(S+1)\right] \\ &+ \frac{1}{\hbar^2} d_{gs}^{\perp}\left[E_x(S_y^2 - S_x^2) + E_y(S_x S_y + S_y S_x)\right] \\ &+ \frac{1}{\hbar}\mu_B g_e \mathbf{S}\cdot\mathbf{B} \end{aligned} \tag{1}$$

where $\hbar$, μ_{B}, and g_{e} are the reduced Planck constant, the Bohr magneton, and the g factor of the electron spin, respectively. **S** is a spin operator and the spin quantum number of the NV center is 1 ($S = 1$). $d_{\mathrm{gs}}{}^{\parallel}/h = 0.35 \pm 0.02$ kHz·cm/kV and $d_{gs}^{\perp}/h = 17 \pm 3$ kHz·cm/kV [36] are the measured axial and non-axial components of the ground triplet state electric dipole moment, respectively. The following Eq. (1) is derived from the spin Hamiltonian described above for the change $\Delta\omega_{\pm}$ of the resonance frequency due to the magnetic field B and the electric field E. However, it is limited to the region where the amount of change in energy is sufficiently smaller

than zero magnetic field splitting $D_{\mathrm{gs}} = 2870$ MHz ($hD_{gs} \gg \mu_B g_e B, d_{gs}^{\perp} E_{\perp}$).

$$\hbar\Delta\omega_{\pm} = d_{gs}^{\parallel} E_z \pm \sqrt{\mu_B^2 g_e^2 B_z^2 + d_{gs}^{\perp 2} E_{\perp}^2} \tag{2}$$

Next, the mechanism of increasing coherence time is explained. Since spin decoherence is caused by fluctuations in the resonance frequency, Eq. (1), which expresses the change in the resonance frequency due to the external field, is important. Looking at the second term of Eq. (1), which is a square root of the sum of the squares of the magnetic field term and the electric field term. In this case, when the contribution of either the electric field or the magnetic field is larger than that of the other, the influence on the resonance frequency of the other becomes smaller. Furthermore, when one is much larger than the other, the resonance frequency hardly changes even if the one with the smaller contribution changes a little. Figure 1.8 shows this relation. When the fluctuation of the resonance frequency due to magnetic noise is the cause of decoherence, it can be expected that the fluctuation of the resonance frequency is suppressed and the coherence time is increased by applying the electric field.

In this research [39], we showed the electrical control for extension of the spin coherence times of 40 nm-deep ion-implanted single NV center spins in diamond by suppressing magnetic noises. NV centers were created by ion implantation and subsequent annealing on a IIa (100) single-crystalline diamond substrate. ^{14}N with a natural abundance concentration (99.6%) was implanted at a depth of about 40 nm by an ion-implantation with a kinetic energy of 30 keV. Electrodes and an antenna to apply an electric field and microwaves, respectively, were formed on the substrate (Fig. 1.9a). From the current–voltage property of the structure to apply an electric field (Fig. 1.9b), it was supposed that the voltage at the interface between the diamond and the electrode was zero and the electric field strength in diamond bulk was linearly proportional to the applied electric field. We applied 120 V DC across two contacts spaced by 10 μm. The spin coherence times, estimated from a free-induction-decay and a Hahn-echo decay, were increased up to about 10 times as shown in Fig. 1.10 and 1.4 times (reaching 150 microseconds), respectively [39].

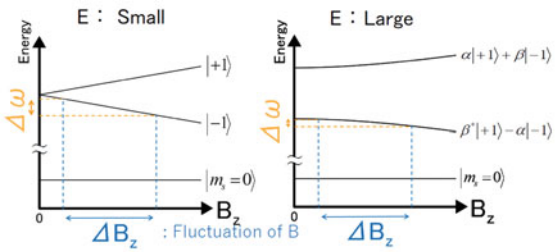

Fig. 1.8 Comparison of the magnitude of resonance frequency fluctuation Δω when the electric field strength is different. The solid line in the figure shows how the energy level of each spin sublevel changes depending on the magnetic field in the z direction. (Left) Under zero electric field. (Right) When electric field large, for example, in the case of E ~ 100 kV/cm

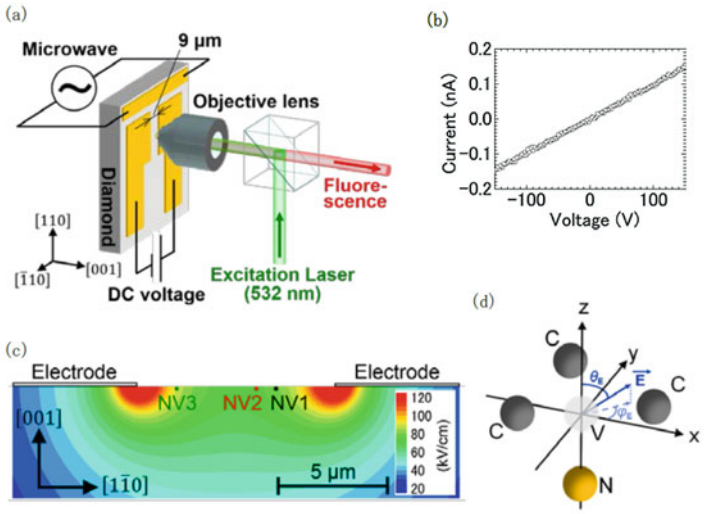

Fig. 1.9 **a** Schematic image of the measurement setup. **b** Current–voltage property between the electrodes on the sample. Linear I-V property is observed. **c** Distribution of the electric field strength in the case where 100 V between the electrodes. Dots marked as NV1, NV2, and NV3 indicate the positions of the NV centers of NV1, NV2, and NV3, respectively. **d** Coordinate system of the NV centers

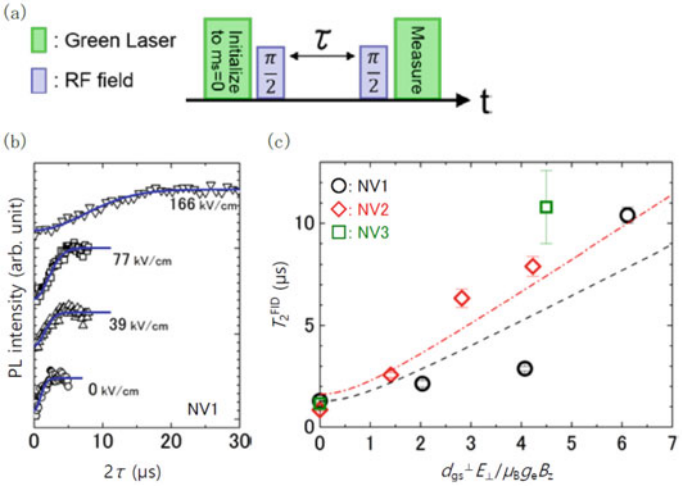

Fig. 1.10 **a** Ramsey pulse sequence to measure $T_2{}^{\mathrm{FID}}$. **b** Decay curves of the Hahn echo signal. Fit function of $f^{echo}(2\tau) = y_0 + A \cdot \exp(-(2\tau/T_2^{echo})^3)$ is employed. **c** Electric field dependence of $T_2{}^{\mathrm{FID}}$. Horizontal axis, which represents the electric field strength, is normalized by the magnetic field along the z-axis. Dashed curve represents the fitted curve for NV1. Chained curve represents the fitted curve for NV2

The electric field dependence of T_2^{FID} and T_2^{echo} at a range up to ~100 kV/cm were quantitatively analyzed based on the spin Hamiltonian. Assuming only a magnetic field fluctuation, the behavior of T_2^{FID} is basically elucidated. The behavior of T_2^{echo} is well reproduced assuming fluctuations in both the electric and magnetic fields. Although the magnetic field fluctuation is the dominant decoherence source for T_2^{FID} in the entire range of the electric field in our experiment and for T_2^{echo} in the low electric field region, the dominant decoherence source for T_2^{echo} in the high electric field region is the electric field fluctuation. The difference in the dominant decoherence source under the electric field is due to the difference in the amplitude–frequency characteristics, corresponding to the difference in the correlation time of the magnetic field fluctuation and the electric field fluctuation in our experiment.

The enhancement of the coherence times by the electric field can contribute to the improvement of the sensitivity in thermometry, pressure and AC electric field sensing, although it is not effective to the magnetic field sensitivity [27]. The present technique can be utilized for not only for the NV center in diamond but also the high-spin centers (S > 1) with the zero-field splitting, such as promising centers in silicon carbide [40, 41]. Our study opens up the new technique of the electrical decoupling of the spin coherence in solid from the magnetic noises.

2.2 *Room Temperature Electrically Detected Nuclear Spin Coherence of NV Centres in Diamond*

We demonstrate electrical detection of the ^{14}N nuclear spin coherence of NV centres at room temperature. Nuclear spins are candidates for quantum memories in quantum-information devices and quantum sensors, and hence the electrical detection of nuclear spin coherence is essential to develop and integrate such quantum devices. In the later section of (1.3.1), hybrid quantum magnetic-field sensor with an electron spin and a nuclear spin to enhance a sensitivity is presented. In the present study, we used a pulsed electrically detected electron-nuclear double resonance technique to measure the Rabi oscillations and coherence time (T_2) of ^{14}N nuclear spins in NV centres at room temperature. We observed $T_2 \approx 0.9$ ms at room temperature. Our results will pave the way for the development of novel electron- and nuclear-spin-based diamond quantum devices.

Nuclear spins in a semiconductor have a long coherence time (T_2) due to the good isolation from environmental noise. Therefore, they are candidates for quantum memories in quantum-information devices and quantum sensors [42–44]. Using nuclear spins (e.g., nitrogen and carbon) in diamond for quantum memories, highly sensitive magnetic sensors, quantum repeaters, quantum registers, etc., have been demonstrated at room temperature. In these demonstrations, the detection of nuclear spin coherence is essential. Nuclear spin coherence can be detected via the electron spins of NV centres, which also have a long T_2 at room temperature. NV electron

spins can be detected by optical techniques and electrical techniques. The electrical technique is an important technology for developing and integrating quantum devices. Furthermore, a theoretical model predicts that its detection sensitivity is approximately three times higher than that of the optical technique [60]. While the photoelectrical detection of the electron spin coherence of an ensemble of NV centres and photoelectrical coherent spin-state readout of single NV centres at room temperature has been demonstrated, the direct electrical detection of nuclear spin coherence remains challenging. Thus, we focus on an electrically detected electron-nuclear double resonance (EDENDOR) technique to demonstrate room-temperature electrical detection of nuclear spin coherence.

Electrical Detection of Nuclear Spin

The first EDENDOR measurement was demonstrated by Stich and collaborators for phosphorus (P) donors in silicon at 4.2 K [45]. After this demonstration, two other groups independently demonstrated pulse EDENDOR measurements of P-donors in silicon [46, 47]. They measured Rabi oscillations and T_2 of P-donor nuclear spins from 3.5 to 5 K. Furthermore, pulsed EDENDOR measurements of proton nuclear spins in organic semiconductors have been demonstrated [48]. Proton nuclear spin resonances have been measured at room temperature, but Rabi and T_2 measurements of proton nuclear spins have not been reported yet. To the best of our knowledge, there have been no demonstrations of room-temperature electrical detection of nuclear spin coherence in diamond or any other materials.

The EDENDOR signals of ^{14}N nuclear-spin coherence are observed by measuring the change in the electrically detected electron-spin echo intensity of the NV centres. The electrically detected magnetic resonance (EDMR) of the NV centres measures the photocurrent change due to electron-spin resonances of the NV centres. The photocurrent can be generated under illumination by a 532-nm laser via a two-photon ionisation process, depicted in Fig. 1.11a. The Fig. shows that the $|\pm1\rangle$ NV electron spin at the ^{3}E state has a transition probability to the long-lived (~220 ns) metastable ^{1}E states, where $|m_s\rangle$ describes an NV electron spin. This causes the photocurrent to decrease due to a magnetic resonance transition from $|0\rangle$ to $|\pm1\rangle$ after the optical

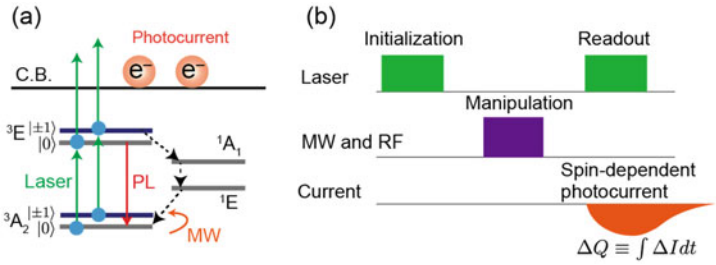

Fig. 1.11 (Colour online) **a** Schematic of the EDENDOR measurements of NV centres in diamond. **b** Process for the EDENDOR measurements

initialisation to $|0\rangle$. Based on this mechanism, this study measures the electron and nuclear spin coherences with the pulse sequence depicted in Fig. 1.11b.

To measure the nuclear magnetic resonance of ^{14}N nuclear spins, we used the Davies ENDOR technique [49]. First, an MW π-pulse is applied to the transition between $|0\rangle$ to $|+1\rangle$ after illumination by a pulsed laser. This π-pulse can generate hyperfine coupling between NV electron spins and ^{14}N nuclear spins and the polarisation between $|+1,0\rangle$ and $|+1,+1\rangle$, where $|m_s,m_I\rangle$ are electron and nuclear spins, respectively. Then, the RF pulse is applied. Finally, ΔQ was measured by applying a Hahn echo sequence and the following laser pulse. We observed EDENDOR spectra by measuring ΔQ as a function of the irradiated RF frequency.

Setting the MW frequency to 2916 MHz, the input MW power to 5 W, and the input RF power to 5 W, we observed the spectrum shown in Fig. 1.12. The observed data can be fitted with the Gaussian function shown by the solid red line in Fig. 1.12. We can estimate that the observed resonance frequency corresponds to the transition between $|+1,0\rangle$ and $|+1,+1\rangle$ of the ^{14}N nuclear spins.

Rabi Oscillations of ^{14}N Nuclear Spins

The top of Fig. 1.13 shows the pulse sequence for the measurements of the ^{14}N nuclear-spin Rabi oscillations. The sequence shows that we measured ΔQ as a function of the length of the RF pulse. Here, we set the MW frequency to 2916 MHz, the input MW power to 5 W, and the RF frequency to 3.5 MHz. The results of the electrically detected nuclear-spin Rabi measurements with four different input RF powers are shown in the bottom of Fig. 1.13. The red, black, blue, and green points correspond to the results with input RF powers of ~2.5, 5, 10, and 20 W, respectively. The observed oscillations are fitted by sinusoidal curves, which are shown as solid lines in the bottom of Fig. 1.13. The results of the curve fittings showed that all

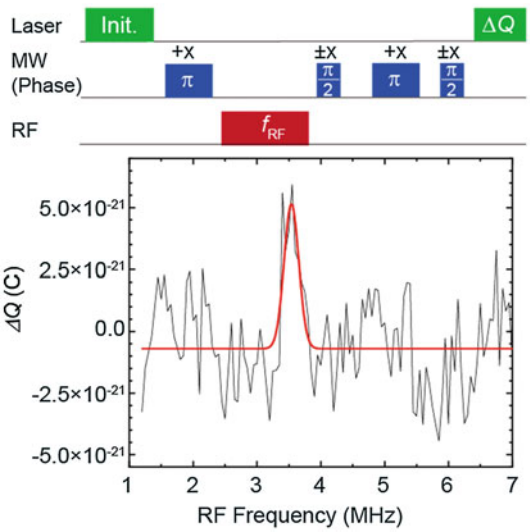

Fig. 1.12 Pulse sequence (top) and the result (bottom) of an electrically detected ENDOR spectrum. $\pm x$ indicate the phase of MW pulse

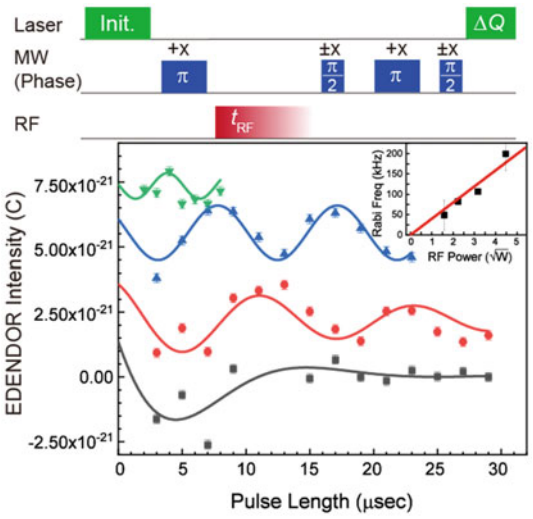

Fig. 1.13 Pulse sequence (top) and the result (bottom) of an electrically detected nuclear Rabi oscillation. $\pm x$ indicate the phase of MW pulse. (Inset) Rabi frequencies as a function of the square root of RF power

Rabi oscillations have the same phase offset which depends on the polarisation of ^{14}N nuclear spin after applying the MW π pulse [49]. Furthermore, the oscillation frequencies observed by the curve fittings are plotted as a function of the square root of the input RF power in the inset of Fig. 1.13. The plots are fitted well by a linear function with the intercept at zero, as shown by the solid line, which certifies that the observed oscillations correspond to Rabi oscillations between $|+1,0\rangle$ and $|+1,+1\rangle$. Hence, the Rabi oscillations of the ^{14}N nuclear spins can be observed with EDENDOR at room temperature.

Echo Decay of ^{14}N Nuclear Spins

In echo decay measurement of ^{14}N nuclear spins, a nuclear-spin Hahn echo sequence was added between the first MW π- and second MW π/2-pulse, allowing the nuclear spin echo intensity to be measured via the change in the ESE intensity. We set the input RF power to 10 W and the other experimental conditions were the same as those for electrically detected nuclear spin Rabi oscillations. Then, we measured ΔQ as a change of the ESE intensity as a function of the freely evolving time of 2τ. From the experimentally observed decay and the fitting with an exponential curve by fixing the echo amplitude at half the Rabi amplitude, consequently, ^{14}N nuclear spin coherence time $T_2^{(n)} \approx 0.9$ (5) ms was estimated [49]. Hence, we successfully observed $T_2^{(n)}$ with the EDENDOR technique at room temperature.

2.3 *Ferromagnetic-Resonance Induced Electromotive Forces in $Ni_{81}Fe_{19}$|p-Type Diamond*

For an electrical control of spin in diamond, we have an interest in the spin current injection to diamond. We report on direct-current (DC) electromotive forces (emfs) in a nickel–iron alloy ($Ni_{81}Fe_{19}$)|p-type diamond under the ferromagnetic resonance of the $Ni_{81}Fe_{19}$ layer at room temperature [50]. The observed DC emfs take its maximum around the ferromagnetic resonant frequency of the $Ni_{81}Fe_{19}$, and their signs are reversed by reversing the direction of an externally-applied magnetic field; it shows that the observed DC emfs are spin-related emfs. The origin of the Lorentzian emfs can be inverse spin-Hall effect in the $Ni_{81}Fe_{19}$|ptype diamond; however, this is still unclear. Additional experiments are required to clarify its origin, e.g., spin-pumping-induced spin transport measurements.

3 Quantum Hybrid Sensors

3.1 *Hybrid Quantum Magnetic-Field Sensor with an Electron Spin and a Nuclear Spin in Diamond*

In this research [51], we propose a scheme to improve the sensitivity of magnetic-field sensors by using a hybrid system of an electron spin and nuclear spin in diamond. The concept is that the electron spin has a strong coupling with the magnetic fields, and so we use this to accumulate the phase from the fields. On the other hand, since the nuclear spin has a longer coherence time than the electron spin, we can store the phase information in the nuclear spin (Fig. 1.14a). By repeating this procedure in

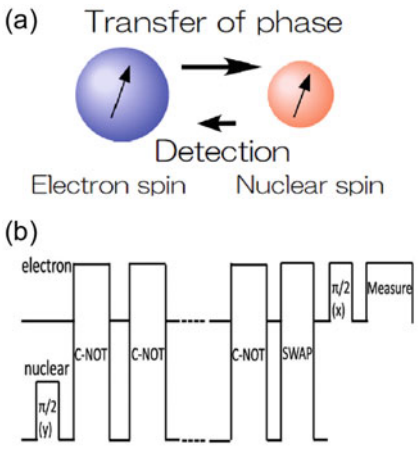

Fig. 1.14 **a** Schemetic image of the method. **b** A pulse sequence to detect magnetic fields with an electron spin and a nuclear spin in the NV center

this hybrid system, we showed that it is possible to detect static magnetic fields with the sensitivity far beyond that of previous sensors using just a single electron spin.

Since the nuclear spin is coupled with an electron spin via a hyperfine coupling, it is possible to transfer the information attained by the electron spin to the nuclear spin for the storage. Actually, a controlled-NOT (C-NOT) gate between the electron spin and the nuclear spin has been already demonstrated in many previous researches [5]. Thus, we can construct an efficient hybrid magnetic-field sensor to combine the preferable properties of these two different systems (Fig. 1.14b).

However, if we consider the effect of decoherence, there is of course a difficulty with this simple picture, namely, a propagation of the error from the electron spin to the nuclear spin. Due to the dephasing effect of the electron spin, the non- diagonal term of the entangled state decreases as quickly as that of the electron spin does. This dephasing error might be accumulated in the nuclear spins, which could destroy the phase information obtained from the target magnetic field. Especially, if the dephasing noise is Markovian, the sensitivity of the hybrid field sensor is as small as that of the conventional one, due to the error propagation. In the Markovian dephasing model, the nondiagonal term of the density matrix decays exponentially. On the other hand, in the case that the relevant dephasing in the NV center is induced by low-frequency noise [22] which is not Markovian, we can suppress the error accumulation. Under the effect of low-frequency noise, the nondiagonal term of the density matrix decays quadratically. Due to this property, the initial decay of the non-Markovian noise is slower than that of the Markovian noise. We numerically evaluated the method and concluded that the sensitivity of our sensor is one order of magnitude better than the conventional one if the gate error is below 0.1% as shown in Fig. 1.15. It should be noted that this can be realized in non-Markovian dephasing model, so it is applicable to low concentration NV center. Note that our scheme can be interpreted as an application of quantum Zeno effect (QZE) [52, 53]. It is known that QZE occurs in a system to show a quadratic decay while QZE cannot be observed for exponential decay process.

We consider that this research is important in the point that it shows the advantage to utilise the quantum hybrid system for quantum sensing in some conditions compared with the conventional method.

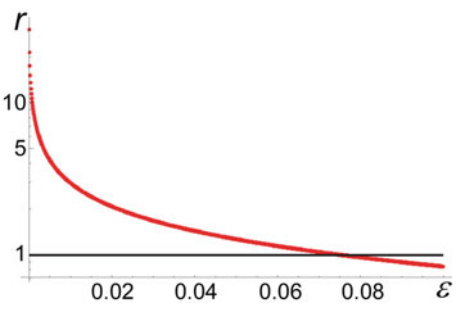

Fig. 1.15 Sensitivity r with respect to the error ε. If the gate error is below 0.1%, the sensitivity of our sensor is one order of magnitude better than the conventional one

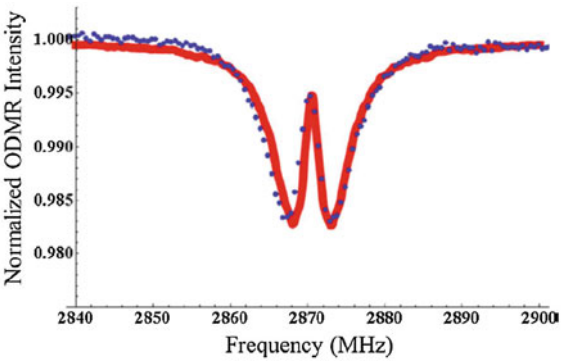

Fig. 1.16 ODMR with zero applied magnetic fields. The red line denotes a numerical simulation and blue dots denote the experimental results

3.2 ODMR of High-Density Ensemble of NV⁻ Centers in Diamond

The ODMR is a way to characterize the NV^- centers. For ultra-high sensitivity, high-density ensemble of NV^- centers are required, therefore, elucidation of a magnetic resonance spectrum of a high-density ensemble of the NV centers are very important. Particularly, for high magnetic field sensitivity, elucidation of it at zero magnetic field is essential. In previous many researches, it is reported that the ODMR spectrum exhibited small splitting with several MHz at zero magnetic field. In most of them, it is simply interpreted that it is due to the strain induced by imperfection of the crystallinity. However, if it is true, most of the NV centers must have a similar strain splitting with each other. In our research, we showed that the small splitting should be interpreted not by the single strain splitting but by strain distributions, inhomogeneous magnetic fields, and homogeneous broadening width [54].

Recently, a remarkably sharp dip was observed in the ODMR with a high-density ensemble of NV centers, and this was reproduced by the previously reported theoretical model [55], showing that the dip is a consequence of the spin-1 properties of the NV^- centers. We showed much more details of analysis to show how this model can be applied to investigate the properties of the NV^- centers. By using our model, we have reproduced the ODMR with and without applied magnetic fields. Also, we theoretically investigate how the ODMR is affected by the typical parameters of the ensemble NV^- centers such as strain distributions, inhomogeneous magnetic fields, and homogeneous broadening width. Our model could provide a way to estimate these parameters from the ODMR, which would be crucial to realize diamond-based quantum information processing.

In addition, by fitting the Hahn echo decay curve with a theoretical model, we showed that both the amplitude and correlation time of the environmental noise have a clear dependence on the spin concentration [56]. These results are essential for optimizing the NV center concentration in high-performance quantum devices, particularly quantum sensors.